

Numerical Simulation and Experimental Study on the Gas-liquid Two-phase Flow in the Pump During the Gas Cut-off Transition Process

F. Yang¹, J. Zhang¹ and C. Shao^{1, 2†}

¹ College of Mechanical and Power Engineering, Nanjing Tech University, Nanjing 211816, Jiangsu, China

² College of Emergency Management, Nanjing Tech University, Nanjing 211816, Jiangsu, China

† Corresponding author, E-mail: chunlei-shao@njtech.edu.cn

ABSTRACT

This study aims at elucidating the flow mechanism and characterizing the internal pump flow properties during the gas cut-off transition process. High-speed photography (HSP) served for visualizing the flow patterns within a transparent centrifugal pump model fabricated from plexiglass. Numerical simulation was conducted on the gas-liquid two-phase flow within the pump in the gas cut-off transition process using the Eulerian-Eulerian heterogeneous flow model coupled with the SST $k-\omega$ turbulence model. The experimental observations from HSP served as validation for the numerical simulation results. During the gas cut-off transition process, with a decreasing gas volume fraction (*GVF*), the pressure in the volute gradually increases until it ultimately exhibits periodic variation. The time-averaged pressure exhibits a steady increase with the flow. The *GVF* slowly diminishes along volute's radial direction. As a consequence of impeller rotation, the outlet pressure rises with the decreasing integral rate of the gas phase inside the impeller. Concurrently, the integral rate at the outlet has not yet changed, so the change in outlet *GVF* consistently lags behind the change in outlet pressure. The centrifugal pump completes the gas cut-off transition process when fluctuations in the outlet *GVF* cease. This investigation revealed the temporal evolution of *GVF* and pressure during the centrifugal pump's gas cut-off transition process, and established a quantitative criterion for determining the completion of this process. The research results are beneficial for more deeply comprehending the pump's performance, and well contribute to the reliable operation and structural optimization pertaining to centrifugal pumps.

Article History

Received January 7, 2025

Revised March 24, 2025

Accepted March 26, 2025

Available online June 3, 2025

Keywords:

Centrifugal pump

Gas-liquid two-phase flow

High-speed photography

Gas cut-off transition process

Numerical simulation

1. INTRODUCTION

Centrifugal pumps enjoy a broad application in military, chemical, agricultural, petroleum, and transportation industries, etc. relying on the concise structure, stable operation and convenient maintenance (Olimstad et al., 2018; Wang et al., 2018; Shao et al., 2019). Many scholars have studied the centrifugal pump in terms of the internal flow and the external characteristics (Zhou et al., 2017; Jia et al., 2019; Li et al., 2020). While centrifugal pumps are predominantly utilized in engineering applications for liquid transport, they occasionally encounter scenarios involving gas-liquid two-phase flow (GLTPF). Under such flow condition, the internal flow becomes substantially more complex, and the gas phase significantly deteriorates pump performance (Yan et al., 2019; He et al., 2020a; Zhao et al., 2021).

Centrifugal pumps run unstably under such flow condition, which significantly compromises their reliability. Zhou et al. (2020) investigated the performance and transient characteristics of centrifugal pumps under such flow conditions. When the gas volume fraction (*GVF*) reached a certain level, the irregular pressure fluctuations was observed. The pressure pulsation intensity at the blade inlet and volute tongue intensified progressively with increasing *GVF*. During start-up, shutdown, and power failure events, centrifugal pumps undergo complex flow transition processes that significantly impact their performance and operational safety (Chalghoum et al., 2016; Li et al., 2018). Fu et al. (2020) numerically simulated and experimentally analyzed the axial flow pump with regard to the transient characteristics. Their findings demonstrated that during pump initiation, key performance parameters including rotational speed, head, and flow rate underwent significant variations. By numerically simulating the

NOMENCLATURE			
b_2	blade outlet width	r_{II}	radius of section II
b_3	volute inlet width	r_{III}	radius of section III
D_2	blade outlet diameter	r_{IV}	radius of section IV
D_3	base circle diameter	r_V	radius of section V
D_g	gas inlet diameter	r_{VI}	radius of section VI
D_l	liquid inlet diameter	r_{VII}	radius of section VII
D_{out}	pump outlet diameter	r_{VIII}	radius of section VIII
D_ω	cross-diffusion term	S_k, S_ω	source term defined by users
f_i	mass force related to impeller rotation	u_i	flow velocity of i phase
G_k	source term of turbulent kinetic energy k	v	velocity
G_ω	source term of dissipation frequency ω	Y_k	diffusion term for turbulent kinetic energy k caused by turbulence
GVF	gas volume fraction	Y_ω	diffusion term for dissipation frequency ω
H	head	Z	blade number
i	any phase	α_i	volume fraction of i phase
L	inlet pipe position	β_{1y}	blade inlet angle
M_i	interface force acting on i th phase	β_{2y}	blade outlet angle
n	rotational speed	η	efficiency
n_s	specific speed	μ_t	turbulent viscosity
p_i	pressure of i phase	μ_i	dynamic viscosity of i phase
p_m	pressure at monitoring point	ρ	density
Q	flow rate	ρ_i	density of i phase
Q_g	gas flow rate	Φ_0	tongue placed angle
Q_l	liquid flow rate	Γ_k/Γ_ω	effective diffusion coefficients of k/ω
r_I	radius of section I		

transient process resulting from centrifugal pump outage, Feng et al. revealed 4 modes of the transient process, i.e. pump mode, braking mode, turbine mode and runaway mode, meanwhile analyzing the internal flow field in the transient process (Feng et al., 2021). Rezaghi and Riasi (2016) examined the hydraulic transient sensitivity with regard to 2 parallel pump turbines in runaway mode, obtaining the transient process variation with modeling parameters. Kan et al. (2020) conducted the unsteady 3D numerical simulation and experiment on the pump full flow system, and studied the tubular pump (instantaneous flow rate and load impact) under the out-of-control condition resulting from power failure. Based on entropy production theory, Feng et al. (2020) quantified energy dissipation by analyzing the distribution of flow field energy losses across various flow passage components during centrifugal pump runaway processes induced by accidental power failure and shutdown events. Zhang (2020) examined temporal variations in rotational speed, flow rate, torque, axial velocity, and velocity moment at the impeller inlet during emergency power-off runaway transitions, while also characterizing the transient flow behavior within diversion pipes and impellers.

As computational fluid dynamics develops, the numerical simulation techniques have emerged as essential tools for analyzing internal flow characteristics within centrifugal pumps. Parikh et al. (2020) selected SST $k-\omega$ turbulence model in conjunction with volume of fluid (VOF) method for the examination of centrifugal pumps' GLTPF behavior. Li et al. (2017) employed the SST $k-\omega$ model to perform 3D incompressible simulations for examining transient characteristics of pump turbines during guide vane closure operations. Their results demonstrated that flow fluctuations were

the primary cause of dynamic instability in both stay and guide vanes. Ge et al. (2020) utilized a coupled CFD-PBM (Computational Fluid Dynamics - Population Balance Model) approach for the simulation of GLTPF dynamics within centrifugal pumps. Zhang et al. (2012) implemented RNG $k-\omega$ turbulence model for numerically simulating centrifugal pump shutdown processes, analyzing transient characteristic variations and unstable flow phenomena throughout the flow domain. Additionally, Zhang et al. (2014) investigated the internal flow patterns and the external characteristics of low specific speed centrifugal pumps during rapid outlet valve closure events (Zhang, et al., 2012, 2014). Wang et al. (2017) conducted numerical simulations using the SST $k-\omega$ model, characterizing the internal flow field of a centrifugal pump with ultra-low specific speed in the transient startup phase and subsequent steady-state operation. Their analysis quantified the effects of varying startup accelerations on the transient impact head, while also elucidating fundamental differences in hydraulic head distribution and internal flow field characteristics between transient and steady-state operating conditions.

Numerous studies have examined the shutdown, power outage, and closing processes in pumps; however, there is a relative scarcity of research focused on the transition from gas on to gas off. The gas cut-off transition (GCOT) process in centrifugal pumps represents the evolution from gas-liquid two-phase flow to single-phase liquid flow after gas injection ceases. and the entire pump system experiences significant hydrodynamic instability. The internal flow field undergoes rapid fluctuations, accompanied by substantial oscillations in critical parameters such as pressure distributions and flow rates. Consequently, it is essential to research the pump's GCOT process. The study

numerically simulates the pump internal flow in the GCOT process using the Eulerian-Eulerian (E-E) heterogeneous flow model together with the SST $k-\omega$ model. High-speed photography (HSP) experiments were conducted for the validation of the numerical simulation results. The pump's transient properties during the GCOT process are the main subject of this investigation. Temporal variations in GVF distributions, pressure fields, and global pump performance characteristics throughout the GCOT process were systematically analyzed. The focus is on studying the series of changes that occur during the sudden cut-off of gas, exploring the impact generated after the sudden cut-off. This phenomenon may also lead to increased vibration and noise inside the pump. The findings in the study assist in optimizing the structures of the GLTPF pump and enhancing its stable operation.

2. NUMERICAL SIMULATION METHOD

2.1 Governing Equations and Turbulence Models

The E-E flow model, as a relatively complex multiphase flow model, serves for simulating GLTPF within the centrifugal pumps (Lee et al., 2015; Yuan et al., 2017). DPM and Euler-Lagrange models can also be applied to gas-liquid two-phase flow, but they are actually more suitable for studying collisions between phases, such as cavitation and wear. The homogeneous flow model can meet the requirement in this study for research problems such as gas belts and bubbles, so after comprehensive consideration, DPM or Euler-Lagrange models were not selected. The continuity and momentum equations dominating the E-E model are as follows (He, 2020b).

Continuity equations:

$$\frac{\partial}{\partial t}(\alpha_i \rho_i) + \nabla \cdot (\alpha_i \rho_i u_i) = 0 \quad (1)$$

Momentum equations:

$$\begin{aligned} \frac{\partial}{\partial t}(\alpha_i \rho_i u_i) + \nabla \cdot (\alpha_i \rho_i u_i \cdot u_i) = \\ -\alpha_i \nabla p_i + \nabla \cdot (\alpha_i \mu_i (\nabla u_i + (\nabla u_i)^T)) \\ + M_i + \alpha_i p_i f_i \end{aligned} \quad (2)$$

where, i represents any phase (liquid or gas), α_i , ρ_i , u_i , p_i , and μ_i are the volume fraction, the density, the flow velocity, the pressure, and the dynamic viscosity of i phase, respectively, M_i represents the interface force acting on i th phase resulting from the presence of other phases, and f_i represents the impeller rotation-related mass force.

Considering the turbulent shear stress, the SST $k-\omega$ model provides sufficiently precise numerical simulation results within the near-wall region to predict flow separation phenomena. Here we predict the centrifugal pump's performance by virtue of the SST $k-\omega$ model (Liu et al., 2013; Kim et al., 2019; Zhao et al., 2018). The

expressions are as follows:

$$\frac{\partial(\rho k)}{\partial t} + \frac{\partial(\rho k u_i)}{\partial x_i} = \frac{\partial}{\partial x_j} \left(\Gamma_k \frac{\partial k}{\partial x_j} \right) + G_k - Y_k + S_k \quad (3)$$

$$\frac{\partial(\rho \omega)}{\partial t} + \frac{\partial(\rho \omega u_i)}{\partial x_i} = \frac{\partial}{\partial x_j} \left(\Gamma_\omega \frac{\partial \omega}{\partial x_j} \right) + G_\omega - Y_\omega + D_\omega + S_\omega \quad (4)$$

$$\mu_t = \rho \frac{k}{\omega} \quad (5)$$

where, ρ represents the density, k is the turbulent kinetic energy, ω represents the dissipation frequency, Γ_k and Γ_ω , G_k and G_ω , Y_k and Y_ω are the effective diffusion coefficient, source term and diffusion term of k and ω , respectively, S_k and S_ω are the user-defined source term, D_ω is the cross-diffusion term, and μ_t is the turbulent viscosity.

2.2 Geometric Model and Mesh Generation

The centrifugal pump has a rated Q , H , and n of 50 m^3/h , 80 m, and 2900 rpm, respectively, and the pump's specific speed is $n_s=47$. The equation for n_s is as follows.

$$n_s = 3.65 \cdot n \frac{Q^{1/2}}{H^{3/4}} \quad (6)$$

Based on Table 1 that lists the pump's primary structural parameters, we constructed the 3D geometric model by virtue of Pro/E 5.0 software (Fig. 1).

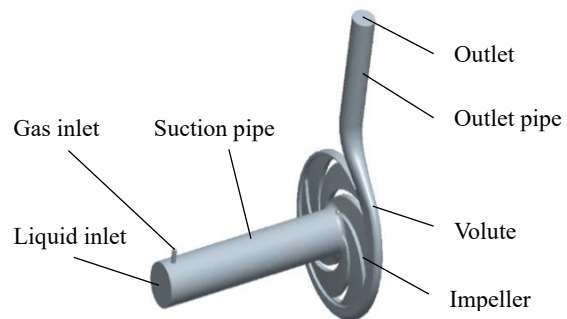


Fig. 1 Geometric model of the pump

With the aim to simulate the real situation, and on the other hand, to ensure the full development of the fluid, thereby avoiding unreliable simulation results, the pump's inlet and outlet pipes were extended.

As illustrated in Fig. 2, ICEM software was employed for the discretization of the flow passages of varying parts. Due to the relatively simple structure of the suction and outlet pipes, hexahedral meshing was implemented for these components. Tetrahedral meshing is highly adaptable to intricate structures and proficient at processing boundaries. Tetrahedral meshing was adopted for the impeller and volute with relatively complex geometry. To optimize computational efficiency while ensuring solution accuracy, the geometric

Table 1. Primary structural parameters of the centrifugal pump

Liquid inlet diameter D_l / mm	Blade outlet width b_2 / mm	Blade inlet angle $\beta_{1y} / ^\circ$
80.0	9	38
Blade outlet angle $\beta_{2y} / ^\circ$	Tongue placed angle $\Phi_0 / ^\circ$	Volute inlet width b_3 / mm
32	20	22
Base circle diameter D_3 / mm	Pump outlet diameter $D_{\text{out}} / \text{mm}$	Blade number Z
260	50.0	6
Blade outlet diameter D_2 / mm	Gas inlet diameter D_g / mm	Position of gas inlet pipe L / mm
250.0	10	450

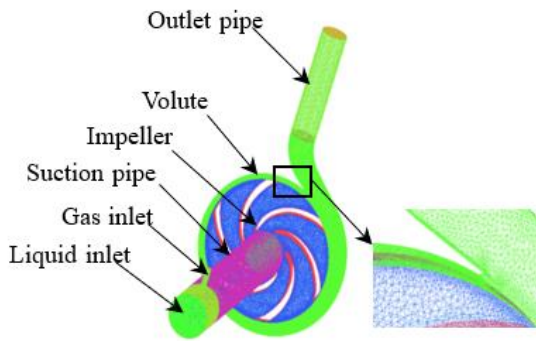


Fig. 2 Grid in calculation domain of the centrifugal pump

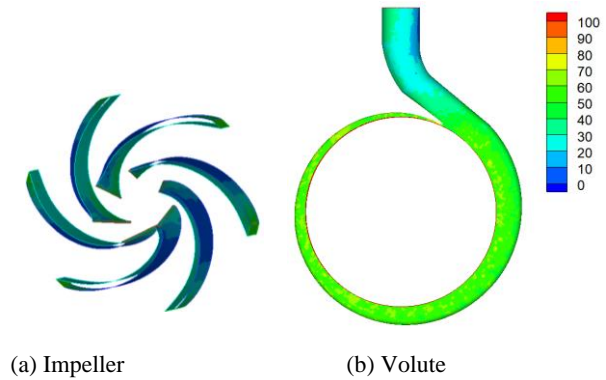


Fig. 4 y^+ distribution on the blade surface and volute surface

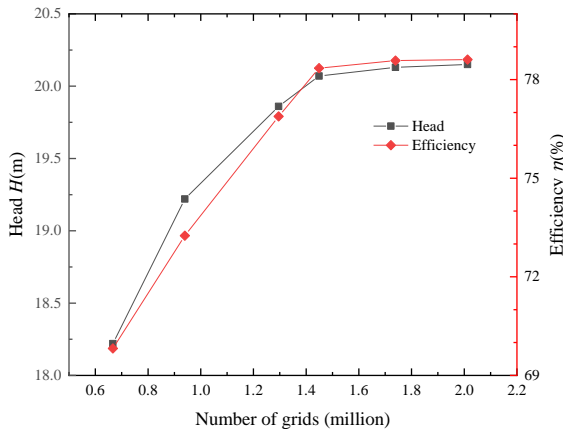


Fig. 3 Effects of different grid numbers on the pump performance

model underwent a grid independence study using 6 different mesh schemes (Fig. 3).

When the mesh count increased from 1,448,920 to 2,012,537 elements, the relative error in head prediction was only 0.40%, while the relative error in efficiency was merely 0.37%. Therefore, the grid number of 1448920 was sufficient. The final mesh distribution consisted of 214,108 elements for the suction pipe, 476,161 for the impeller, 19,000 for the outlet pipe, and 739,651 for the volute. Grid cells have a minimum orthogonal quality > 0.4 .

For ensuring the simulation accuracy, the SST $k-\omega$ model should engage in minimizing the value of y^+ to guarantee at least $y^+ \leq 100$ (Li et al., 2012). Figure 4 depicts the way y^+ is distributed on the blade and volute surfaces. y^+ has an average value < 100 . Hence, the quality of the grid satisfies the requirements.

2.3 Calculation Method and Boundary Conditions

(1) Calculation methods

We employed the E-E model for the numerical simulation of the GLTPF under the assistance of ANSYS Fluent 16.0, selected the SST $k-\omega$ two-equation turbulence model, implemented the Schiller-Naumann model to account for the interfacial drag between gas and liquid phases, and set the gravitational acceleration to 9.81 m/s^2 (Yu & Liu, 2013).

(2) Boundary conditions

For the transient simulation, the velocity inlet boundary condition was utilized for the volumetric inlet. Setting $50 \text{ m}^3/\text{h}$ as the liquid flow rate Q_l , 80 mm as the hydraulic diameter, and 40 L/min for the gas inlet flow rate Q_g , and 10 mm for the hydraulic diameter. The inlet GVF was set as 4.5%. The outlet boundary was defined as an outflow condition, while all walls were no-slip solid boundaries. The impeller rotational speed was 2900 rpm.

(3) Initial conditions

The time step was $5.7471 \times 10^{-5} \text{ s}$, corresponding to the angular displacement of one degree per impeller

revolution. The converged transient solution with an inlet *GVF* of 4.5% was adopted as the initial condition. Subsequently, the inlet *GVF* abruptly decreased to 0% to accurately simulate the GCOT process.

2.4 Monitoring Points

Strategic monitoring points were established at critical locations within the centrifugal pump to monitor both the periodic transient flow behavior and the evolution of GLTPF characteristics during the GCOT process, for monitoring the temporal variations of key parameters including velocity, pressure, and *GVF*, thereby elucidating the evolutionary trends of the internal flow field. Figure 5 illustrates the eight characteristic sections of the centrifugal pump, while Fig. 6 depicts the monitoring points' spatial distribution, where, the designation "pi" represents the pump inlet, with the subsequent numerical value indicating the axial distance (in mm) the monitoring point and the center cross-section of the pump. Similarly, "po" denotes the pump outlet, with the associated numerical value representing the radial distance (in mm) between the monitoring point and the inlet pipe centerline of the centrifugal pump.

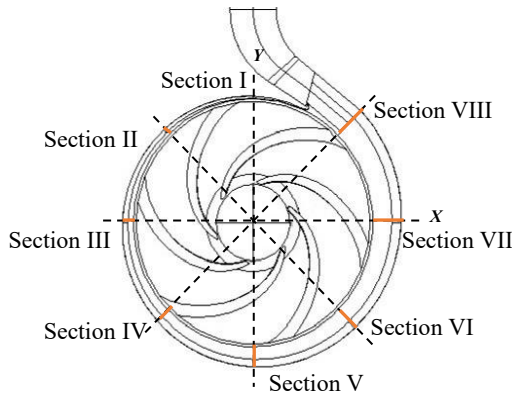


Fig. 5. Eight sections of the volute

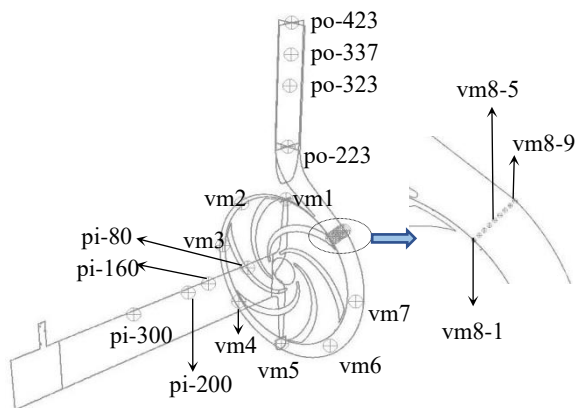


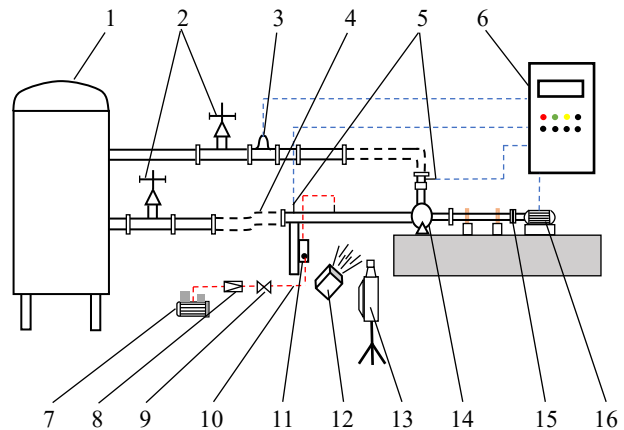
Fig. 6. Location of the monitoring points

3 EXPERIMENTAL DEVICE AND METHOD

3.1 Experimental Device

The experimental apparatus was employed for the

examination of the GCOT process in the centrifugal pump (Fig. 7). The system operates as a closed loop wherein the centrifugal pump draws clean water from the storage tank and recirculates it back through a sequence of components: inlet regulating valve, metal hose, inlet pressure transducer, model pump, outlet pressure transducer, turbine flowmeter and outlet regulating valve. Compressed air from the air pump is regulated by virtue of a reducing valve, metered via a gas control valve and rotameter, and subsequently injected into the suction pipe. This air-water mixture flows through the pump system before ultimately separating in the water storage tank, with air being vented from the top of the tank.



1. Water storage tank; 2. Inlet and outlet regulating valve; 3. Turbine flowmeter; 4. Metal hose; 5. Inlet and outlet pressure transducer; 6. Control cabinet; 7. Air pump; 8. Pressure reducing valve; 9. Gas control valve; 10. Hose; 11. Rotameter; 12. Cold light source; 13. High-speed camera; 14. Model pump; 15. Coupling; 16. Motor

Fig. 7 Schematic diagram of the test device

The model pump has an internal flow passage geometry the same as a low specific speed centrifugal pump (IS 80-50-250, Fig. 8). The experimental pump housing was fabricated from transparent plexiglass to facilitate direct visualization of the two-phase flow phenomena within the internal passages.

We measured the inlet and outlet pressures pertaining to the centrifugal pump using two calibrated WT200 pressure transducers with measurement ranges of -100 to 100 kPa and 0 to 1.2 MPa, respectively, both featuring a measurement accuracy of $\pm 0.1\%$ full scale.

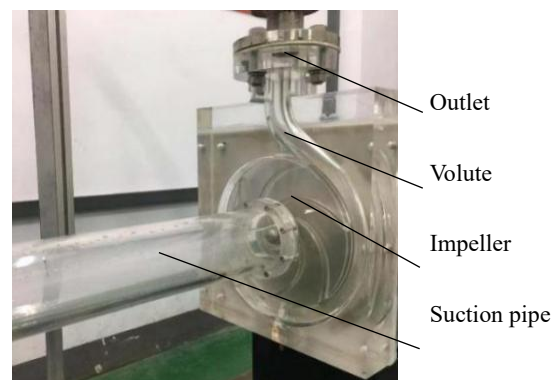


Fig. 8 Model pump

Gas flow rates were quantified using an LZB-6WB rotameter with a full-scale capacity of 40 L/min and a reading accuracy of $\pm 1.5\%$ full scale. Liquid volumetric flow was measured using an LWGY-50A0A3T turbine flowmeter with a measurement range of 0-40 m³/h and a calibrated accuracy of $\pm 0.5\%$ of the measured value. The frequency converter within the control cabinet takes charge of managing the pump rotational speed.

3.2 Experimental Method

Taking air and clean water as media, we experimentally measured the external characteristics of the centrifugal pump according to the methodology (Shao et al., 2015). After ensuring all experimental preparations were complete, we opened the inlet valve and started the motor, and set the pump rotational speed to 600 rpm taking into consideration the structural integrity of the plexiglass model pump. The outlet valve was regulated to adjust the initial liquid flow rate to 15 m³/h. After the operation stabilized, the air pump was activated, with the gas flow rate at 7.5 L/min. When the GLTPF in the pump reached steady-state conditions, the gas source was terminated and the two-phase flow dynamics during the GCOT process was imaged using the high-speed camera.

A high-speed camera (i-SPEED 3) recorded the flow in the impeller and suction pipe to analyze the GLTPF behavior regarding the centrifugal pump. According to Fig. 9(a) illustrating the camera's positioning for capturing the impeller and volute flow, the centrifugal pump's central cross-section was oriented perpendicular to the camera optical axis. The distance between the midplane of the pump and the camera lens was maintained at 0.4 meters. The field of view was around 205mm \times 165mm, the shooting frequency was 1,000 frames/s, and the image resolution was 1,280 \times 1,024. Due to buoyancy effects, bubbles within the pump tend to rise upward; therefore, imaging the pipeline along the horizontal direction provided better visualization of bubble distribution. Figure 9 (b) illustrates the position of the high-speed camera for capturing the internal flow patterns within the suction pipe. The captured images encompassed a region extending 300 mm upstream of the impeller inlet. To ensure optimal image clarity, an HLS-30 LED light source operating at 250 W was utilized to illuminate the observation region.

4. RESULTS AND DISCUSSION

4.1 Experimental and Simulated Results Comparison

4.1.1 Temporal Gas Distribution in the Suction Pipe

After the gas source has been cut off, the time-dependent gas distribution underwent experimental analysis and numerical simulation (Figs. 10 and 11). As illustrated in Figs. 10(a) and 11(a), at the moment of gas source termination ($t = 0$ s), the flow pattern remains steady and identical to the conditions observed prior to the gas cut-off. The gas phase predominantly migrates along the upper wall, forming a gas layer of uniform width (Fig. 10(a)). The gas and liquid phases in the suction pipe exhibit stratified flow behavior, with no dispersed bubbles observed in the vicinity of the gas layer. This stratification phenomenon can be attributed to the

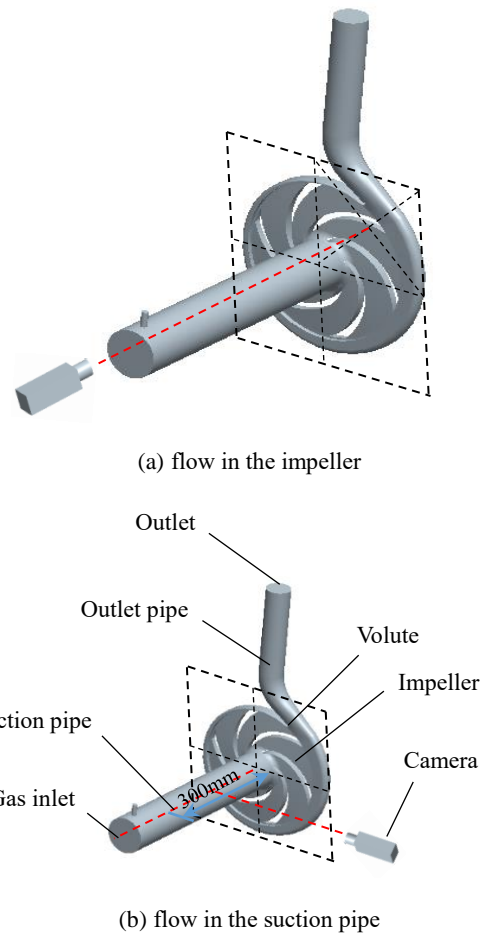


Fig. 9 Shooting region of the centrifugal pump and camera

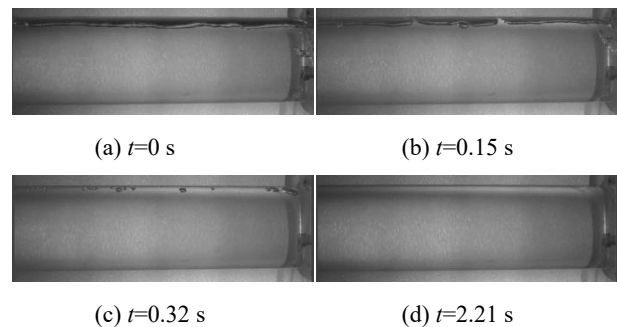


Fig. 10 Temporal gas distribution in the suction pipe

relatively low flow velocity and moderate turbulence intensity within the pipe, which stabilizes the formed gas layer and inhibits bubble dispersion.

At a time $t = 0.15$ s, the continuous gas layer in the suction pipe fragments into multiple smaller gas segments of varying lengths. Concurrently, several dispersed bubbles appear in the vicinity of these gas segments, as illustrated in Figs. 10 (b) and 11 (b). This fragmentation phenomenon results from small quantities of gas detaching from the primary gas layer and forming discrete bubbles due to the turbulent fluctuations of the fluid within the pipe.

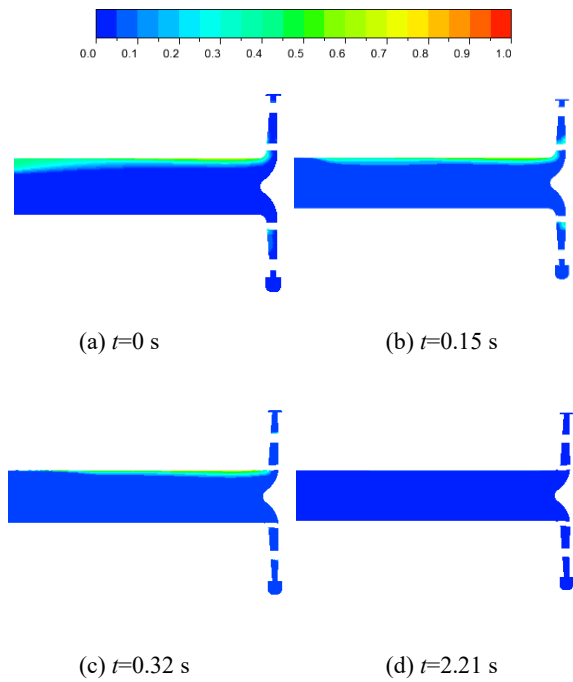


Fig. 11 Temporal GVF distribution in the suction pipe

As the process evolves, gas segments of various lengths progressively enter the impeller entrained by the liquid flow. Consequently, only a limited number of ellipsoidal bubbles remain in the suction pipe, with their size and concentration gradually diminishing. At a time of 0.32 s, the gas distribution within the suction pipe is depicted in Figs. 10 (c) and 11 (c). This evolution in bubble morphology can be attributed to the progressive reduction in gas volume within the suction pipe after the gas supply terminates. This decreased gas volume subsequently reduces the probability of bubble coalescence and interactions. At this stage, the gas is exclusively observable in the form of discrete bubbles. Due to buoyancy effects, these bubbles predominantly accumulate at the suction pipe's upper region.

The remaining small bubbles, entrained by the liquid flow, rapidly migrate into the impeller. Without additional gas supply, the suction pipe becomes completely void of gas within a brief time interval. This marks the completion of the GCOT process in the suction pipe. Figures. 10 (d) and 11 (d) depict the flow stage when $t = 2.21$ s.

4.1.2 Temporal Gas Distribution in the Impeller and Volute

According to Fig. 12 and 13 that illustrate the gas distribution evolution during the GCOT process, as acquired from both experimental measurements and numerical simulations, at the moment of gas source termination ($t = 0$ s), the flow patterns remain unaffected by the cessation of the gas supply. Consequently, there is no discernible distinction between the flow conditions at the initial moment of gas cut-off and those during continuous gas injection (Figs. 12(a) and 13(a)). In Fig. 12(a), there are numerous bubbles distributed throughout both the volute and impeller. Bubble diameters within the volute are significantly smaller than those within the impeller, exhibiting a gradual decrease along the volute's

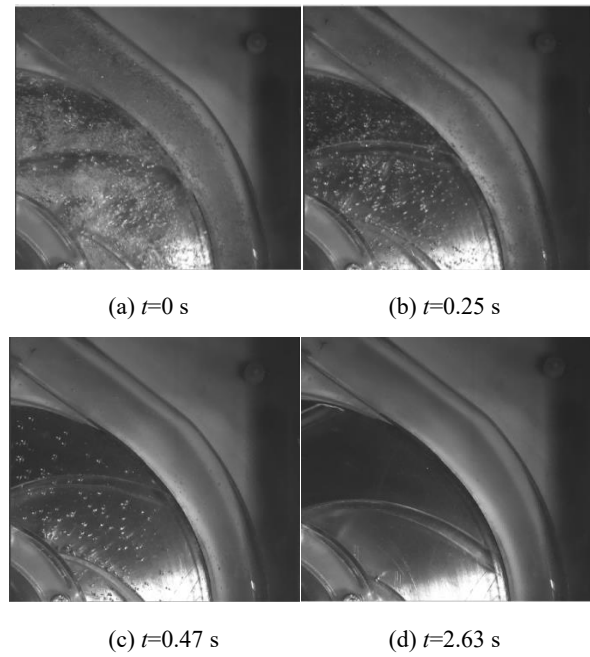


Fig. 12 Temporal gas distribution in the volute and impeller

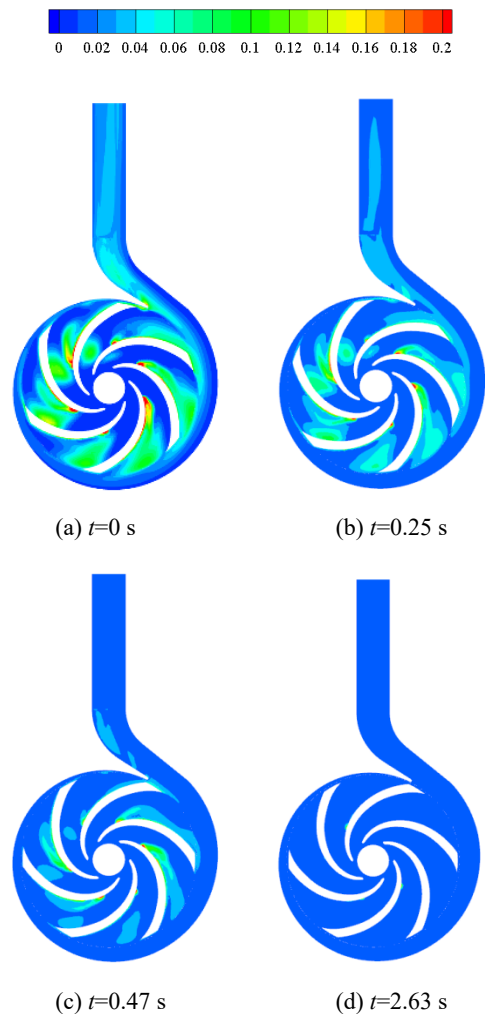


Fig. 13 Temporal GVF distribution in the volute and impeller

radial direction. The region adjacent to the volute wall is characterized by an almost complete absence of bubbles. This is because of the pressure gradient increase in the radial direction.

As the impeller continues to rotate, gas is continuously transported from the impeller into the volute and subsequently toward the pump outlet. Figures 12 (b) and 13 (b) illustrate the flow stage at a time of $t = 0.25$ s. Following the gas source termination, the gas supply becomes progressively insufficient (Fig. 12(b)). Consequently, both the concentration and size of the bubbles within the impeller exhibit a gradual reduction, while the inter-bubble spacing increases. This increased spacing results in reduced bubble collision frequency, transforming the bubble arrangement from clustered aggregations to a dispersed distribution.

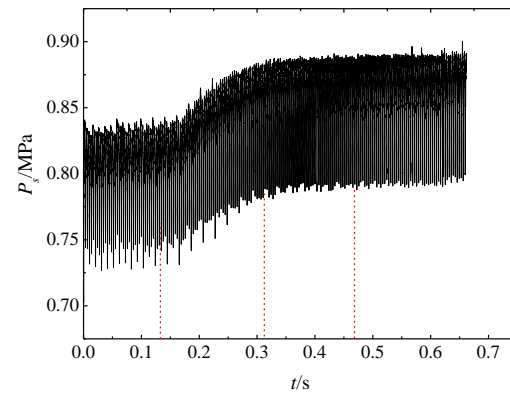
Due to the impeller's rotation, bubbles are transported with the liquid phase to the volute under centrifugal forces. Consequently, the bubble population within the impeller progressively diminishes. Simultaneously, bubbles within the volute are conveyed with the fluid toward the pump outlet, leading to a gradual reduction in their concentration. Figure 12 (c) and 13 (c) show the flow stage at a time of $t = 0.47$ s. Most bubbles within the impeller exhibit irregular ellipsoidal morphologies, while only a minor fraction maintain spherical geometries (Fig. 12 (c)). Bubble diameters exhibit a systematic decrease along the impeller's radial direction. This bubble size gradient primarily results from the increasing pressure field in the radial direction.

The transition process progresses with the rapid evacuation of all remaining bubbles in the impeller and volute from the system. This point marks the completion of the GCOT process, with the pump returning to single-phase flow operation, as illustrated in Figs. 12 (d) and 13 (d).

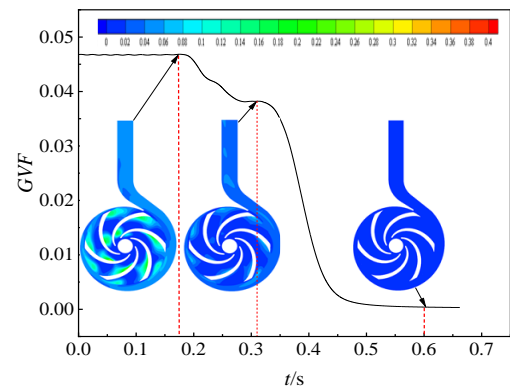
According to the comparison results of experimental and numerical data for the suction pipe, impeller, and volute at corresponding time points, despite experimental limitations in quantitatively measuring *GVF* distribution, both approaches demonstrate consistent qualitative gas distribution patterns and evolutionary trends. Therefore, under the operating conditions investigated in this study, numerical simulation methodology demonstrates its validity as a reliable alternative to experimental approaches for investigating flow behavior within centrifugal pumps. Consequently, subsequent analyses in this study are conducted using validated numerical simulation methods under the specified operating conditions.

4.2 Judgment Criteria for the End of the GCOT process

To determine the end of the GCOT process, the pump outlet pressure and *GVF* were continuously monitored. Figure 14(a) and 14(b) depict the temporal variation of pump outlet pressure and pump outlet *GVF*, respectively. For analytical convenience, the moment of gas cut-off was designated as the initial time ($t = 0$ s). In Fig. 14 (a), In the case of $t < 0.13$ s, the pressure fluctuation at the pump outlet remains essentially identical to that under gas injection conditions, exhibiting no significant



(a)



(b)

Fig. 14 Temporal variation of the pump outlet pressure and *GVF*

changes. In the cases of $0.13 \text{ s} < t < 0.31 \text{ s}$, $0.31 \text{ s} < t < 0.46 \text{ s}$, and $t > 0.46 \text{ s}$, the pump outlet pressure exhibits a fast increase, a slow increase and a periodical fluctuation, respectively. As evident in Fig. 14 (b), in the case of $t < 0.17 \text{ s}$, the pump outlet *GVF* has no obvious change. When $0.17 \text{ s} < t \leq 0.6 \text{ s}$, with the continuous reduction of *GVF* in the pump, the outlet *GVF* decreases continuously. In the case of $t > 0.6 \text{ s}$, the outlet *GVF* is zero.

Based on the aforementioned observations, it can be inferred as follows: When operating at inlet *GVF*s below the critical threshold, the pump outlet pressure begins to demonstrate stable periodic fluctuations while the outlet *GVF* continues to decrease gradually, not yet reaching zero. The response of outlet *GVF* consistently demonstrates a temporal delay relative to changes in outlet pressure. This phenomenon occurs primarily because outlet pressure variations are predominantly influenced by impeller rotation dynamics. As the *GVF* within the impeller decreases, the outlet pressure commences its increase, while the *GVF* at the outlet initially remains temporally invariant. Therefore, it is more precise to establish the moment when the outlet *GVF* stabilizes at zero as the definitive criterion to ascertain the conclusion of the GCOT process.

4.3 Temporal Variation of *GVF* in the Pump

4.3.1 Temporal Variation of *GVF* in the Suction Pipe

Monitoring points were strategically positioned near

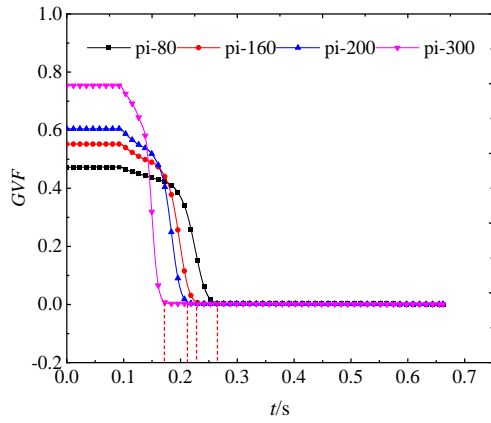


Fig. 15 Temporal *GVF* variation in the suction pipe

the suction pipe’s upper wall, where gas preferentially accumulates under buoyancy effects. According to Fig. 15, *GVF* at all monitoring points presents a consistent temporal variation profile. The evolution is characterized by initial subtle changes, followed by gradual decreases, and eventually stabilization at equilibrium values. Prior to gas cut-off, buoyancy forces drive the progressive accumulation of gas toward the suction pipe’s upper region following the flow path, resulting in substantial gas accumulation above these points. Therefore, the monitoring points near the impeller exhibits a smaller *GVF* versus those far away from the impeller.

Following gas source termination, the *GVF* in the suction pipe gradually decreases temporally after the gas source is cut off. The temporal point at which the *GVF* diminishes to zero (complete gas elimination) varies across the different monitoring locations. At a time t of 0.17 s, the monitoring point pi-300 does not exhibit the presence of any gas. The time of gas unavailability at pi-200, pi-160, and pi-80 is recorded as 0.21 s, 0.23 s, and 0.26 s, respectively. Gas evacuation proceeds sequentially from the most upstream location (pi-300) to the most downstream location (pi-80) proximal to the impeller inlet. This sequential evacuation pattern results from the continuous entrainment of gas by the liquid flow into the impeller, while concurrently no additional gas enters the suction pipe. The GCOT process within the suction pipe concludes when the *GVF* reaches zero, with the complete transition requiring approximately 0.26 s.

4.3.2 Temporal Variation of *GVF* on Sections I~VIII

Figure 16 (a) ~ (h) depicts the temporal evolution of the *GVF* at each monitoring point on sections I~VIII.

Across the various monitoring locations, the *GVF* exhibits a consistent temporal pattern. Initially, there is periodic fluctuation, followed by a quick reduction, then a steady decrease, and ultimately reaching a value of zero. Although monitoring points vm1 through vm8-5 demonstrate comparable temporal trends in *GVF*, significant differences exist in their fluctuation amplitudes. The monitoring point vm1 is located in the closest proximity to the impeller’s outer periphery and near the volute tongue, where the flow exhibits intricate characteristics. Consequently, this location exhibits

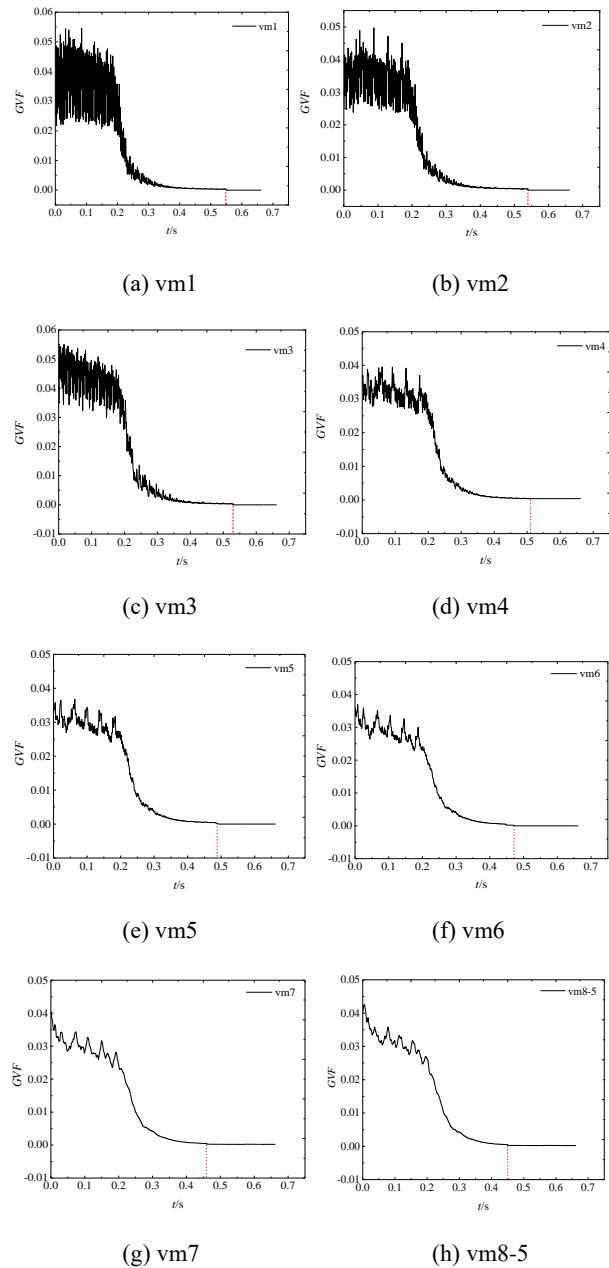


Fig. 16 Temporal *GVF* variation on sections I~VIII

significantly higher *GVF* fluctuation amplitudes compared to other monitoring positions. Proceeding from vm1 toward vm8-5, the increasing radial distance from the impeller’s outer periphery corresponds to a progressive attenuation of impeller-induced flow effects. This spatial trend manifests as systematically decreasing amplitudes of *GVF* fluctuations with increasing distance from the impeller.

Immediately following gas source termination, the *GVF* at all monitoring points exhibits periodic fluctuations without significant reduction, attributable to the continued presence of gas within the volute. With the temporal flow evolution, the *GVF* at each monitoring point decreases periodically. From monitoring point vm1 to vm8-5, the gas disappearance time is 0.55 s, 0.54 s, 0.53 s, 0.51 s, 0.49 s, 0.47 s, 0.46 s and 0.45 s at each monitoring point, respectively. Since the gas is gradually

carried away from the volute by the liquid along the flow direction, no additional gas is subsequently introduced, the gas at each monitoring point eventually disappears. According to pump theory, the fluid in the volute flows from the section I to VIII, with the gas flowing with the liquid. The *GVF* at monitoring point vm1 should be the first to reach 0. However, this stands in direct contrast to the occurrence that has been seen. The underlying cause of this occurrence can be attributed to the following factors: The *GVF* exhibits a slow decrease along the radial direction of the volute. From vm1 to vm8-5, with an enlarging distance from the impeller outlet to each monitoring point, gas penetration to these monitoring points becomes progressively more difficult. Consequently, the *GVF* at the monitoring point vm8-5 first attains a value of 0.

With the *GVF* in the volute reaching 0, the GCOT process in the volute ends, and the time required is about 0.55 s.

4.4 Temporal Pressure Variation In The Pump

4.4.1 Pressure Variation on the Sections I~VII

Figure 17 illustrates the pressure variations p_m across sections I~VII. After the gas source is cut off, the pump remains in the GLTPF state (Fig. 17(a)). Initially, the pressure fluctuates for a period of time. As the *GVF* steadily decreases, the pressure at all monitoring points increases progressively. When the GCOT process completes, the pressure displays periodic fluctuations.

Figure 17 (b) ~ (h) are partial enlarged views of Fig. 17 (a). The pressure fluctuation amplitudes at vm1-7 are 0.19, 0.12, 0.05, 0.045, 0.04, 0.035, and 0.025 MPa, respectively. The amplitude of pressure fluctuations at monitoring points vm1 to vm7 steadily diminishes as these points are located at increasing distances from the impeller outlet. Consequently, the impeller-induced interference effect attenuates. The time-averaged pressure rises monotonically from vm1 to vm7, demonstrating a gradual pressure rise along the flow direction within the volute, conforming to the fundamental design principles of centrifugal pumps.

In conclusion, the time-averaged pressure rises progressively along the flow direction, while the pressure fluctuation amplitude is predominantly governed by impeller interference.

Figure 18(a) reveals that the pressure fluctuation pattern is fundamentally similar to that observed at sections I~VII. Initially, the pressure increases gradually before eventually establishing periodic fluctuations. Fig. 18 (b), the partial enlarged view of Fig. 18 (a), reveals the monotonic increase of the time-averaged pressure at vm8-1 to vm8-9 along the volute's radial direction, conforming to the established pressure distribution principles within volute structures. Both pressure fluctuation amplitude and phase angle remain largely consistent, indicating synchronized pressure variations throughout this region.

5 CONCLUSIONS AND PROSPECTS

5.1 Conclusions

(1) Although experimental methods cannot precisely

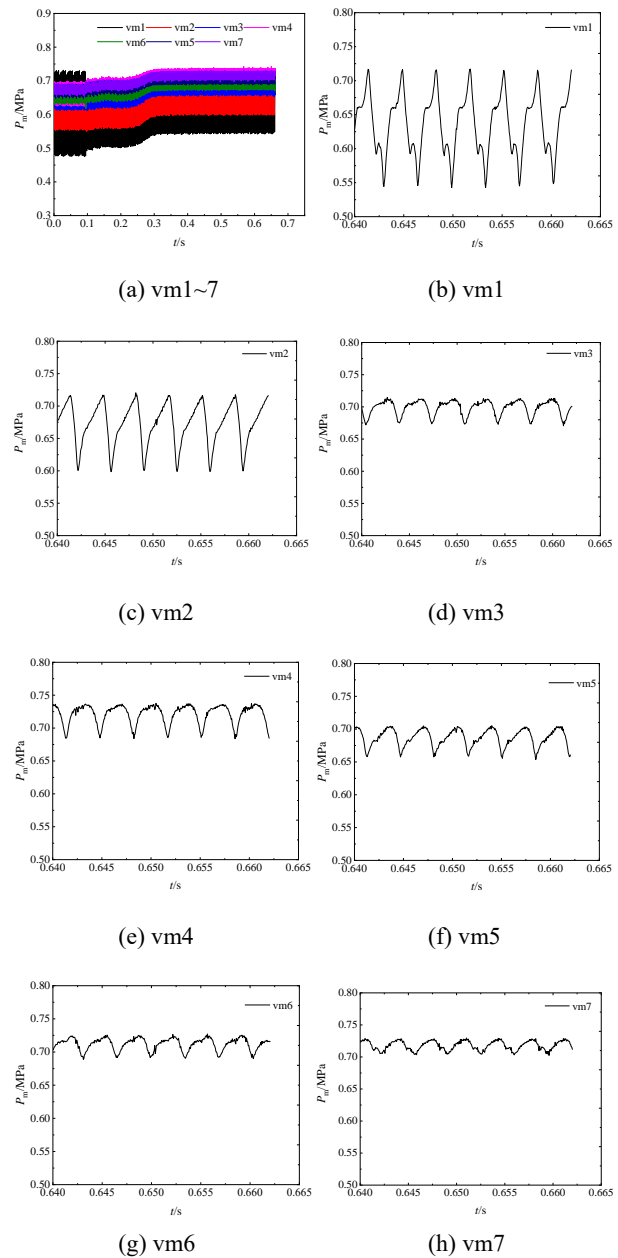
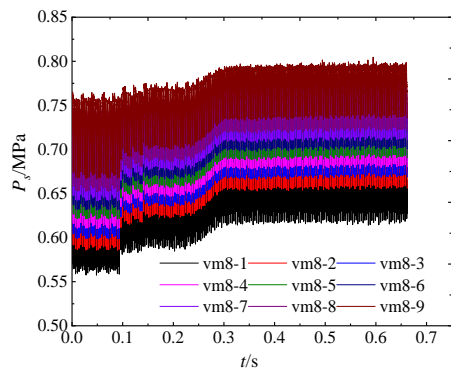


Fig. 17 Temporal pressure variation on the sections I~VII

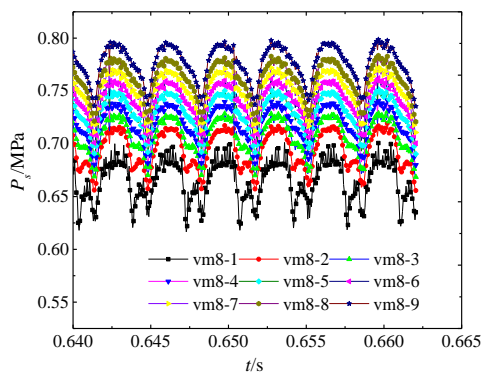
determine the *GVF* at specific locations within the pump, comparative analysis on experimentally observed bubble distributions and numerically simulated *GVF* distributions at corresponding positions reveals consistent trends between experimental and simulation results.

(2) The outlet pressure exhibits a strong correlation with the *GVF* in the impeller. The change of the outlet *GVF* always lags behind the change of the outlet pressure. Therefore, stabilized outlet *GVF* provides a more reliable criterion for determining the completion of the GCOT process.

(3) Following gas source termination, gas present at monitoring points in the suction pipe disappears progressively with flow. Within the volute, the *GVF* fluctuation amplitude declines progressively from vm1-vm8-5, corresponding to the increasing distance



(a)



(b)

Fig. 18 Pressure variation on the section VIII

between monitoring points and the impeller periphery. Moreover, when gas content in the volute is reduced, it is more difficult for the gas to reach the position far from the impeller outlet, so the *GVF* on the monitoring point vm8-5 reaches 0 first.

(4) The time-averaged pressure presents a monotonic increase along with the flow direction, and the impeller interference predominantly impacts the pressure fluctuation amplitude. Pressure fluctuation amplitude at monitoring points is in inverse proportion to their distance from the impeller outlet. Along the volute's radial direction, the pressure fluctuation amplitude and phase angle are basically the same, indicating that the pressure change is timely.

5.2 Prospects

(1) Some conclusions in this article do not have a comparison between experimental and simulation results, such as Figure 16 and Figure 17. This is due to the limitations of experimental equipment and the difficulty of experimental feasibility. Appropriate methods will be sought to conduct experiments to verify these simulation results in the future.

(2) In other working conditions where severe cavitation may occur, the changes in cavitation during GCOT process may also be a direction for further research.

ACKNOWLEDGMENTS

The work was supported by Postgraduate Research & Practice Innovation Program of Jiangsu Province (Grant No. SJCX25_0606), Open Sharing Research Project for Large Scientific Instruments of Nanjing Tech University (Grant No. DYGX20240001), Self-made Experimental Instruments and Equipment Project of Nanjing Tech University (Grant No. ZZYQ202407), Education and Teaching Reform Project of Nanjing Tech University (Grant No. YJG2411).

References

- Chalghoum, I., Elaoud, S., Akrouf, M., & Taieb, E. H. (2016). Transient behavior of a centrifugal pump during starting period. *Applied Acoustics*, *109*, 82-89. <https://doi.org/10.1016/j.apacoust.2016.02.007>
- Feng, J. J., Ge, G., Zhang, Y., Zhu, G. J., Wu, G. K., Lu, J. L., & Luo, X. Q. (2021). Numerical investigation on characteristics of transient process in centrifugal pumps during power failure. *Renewable Energy*, *170*, 267-276. <https://doi.org/10.1016/j.renene.2021.01.104>
- Feng, J. J., Zhang, Y., Zhu, G. J., Li, Y. Z., Li, W. F., & Luo, X. Q. (2020). Transition process characteristics of centrifugal pump with power-off based on entropy production theory. *Transactions of the Chinese Society of Agricultural Engineering*, *36*(4), 10-17. <https://doi.org/10.11975/j.issn.1002-6819.2020.04.002>
- Fu, S. F., Zheng, Y., Kan, K., Chen, H. X., Han, X. X., Liang, X. L., Kiu, H. W., & Tian, X. Q. (2020). Numerical simulation and experimental study of transient characteristics in an axial flow pump during start-up. *Renewable Energy*, *146*, 1879-1887. <https://doi.org/10.1016/j.renene.2019.07.123>
- Ge, Z. G., He, D. H., Huang, R., Zuo, J. L., & Luo, X. Q. (2020). Application of CFD-PBM coupling model for analysis of gas-liquid distribution characteristics in centrifugal pump. *Journal of Petroleum Science and Engineering*, *194*, 107518. <https://doi.org/10.1016/j.petrol.2020.107518>
- He, D. H., Ge, Z. G., Bai, B. F., Guo, P. C., & Luo, X. Q. (2020a). Gas-liquid two-phase performance of centrifugal pump under bubble inflow based on computational fluid dynamics-population balance model coupling model. *Journal of Fluids Engineering*, *142*(8), 081402. <https://doi.org/10.1115/1.4047064>
- He, W. T. (2020b). *Numerical simulations on gas-liquid two-phase flow characteristics of centrifugal pumps with models considering for different bubbles variations*. Zhen Jiang, Jiangsu University. <https://doi.org/10.27170/d.cnki.gjsuu.2020.001519>.
- Jia, X. Q., Yuan, S., Zhu, Z. C., & Cui, B. L. (2019). Numerical study on instantaneous radial force of a centrifugal pump for different working conditions. *Engineering Computations*, *37*(2), 458-480.

- <https://doi.org/10.1108/EC-04-2019-014>
- Kan, K., Zheng, Y., Chen, X., Zhou, D. Q., Dai, J., Binama, M., & Yu, A. (2020). Numerical simulation of transient flow in a shaft extension tubular pump unit during runaway process caused by power failure. *Renewable Energy*, *154*, 1153-1164. <https://doi.org/10.1016/j.renene.2020.03.057>
- Kim, J. H., Cho, B. M., Kim, S., Lee, Y. K., & Choi, Y. S. (2019). Detailed flow characteristic analysis of a three-stage centrifugal pump at design and off-design conditions. *IOP Conference Series: Earth and Environmental Science*, *240*, 092004. <https://doi.org/10.1088/1755-1315/240/9/092004>
- Lee, H. C., Yoo, I. S., Kim, J. H., Kim, J. Y., Yoon, J. Y., Choi, W. C., & Choi, Y. S. (2015). Improvement of hydrodynamic performance of a multiphase pump using design of experiment techniques. *ASME. Journal of Fluids Engineering*, *137*(8), 081301. <https://doi.org/10.1115/1.4029890>
- Li, D. Y., Wang, H. J., Li, Z. G., Nielsen, T. K., Goyal, R., Wei, X. Z., & Qin, A. Q. (2017). Transient characteristics during the closure of guide vanes in a pump turbine in pump mode. *Renewable Energy*, *118*, 973-983. <https://doi.org/10.1016/j.renene.2017.10.088>
- Li, W., Zhang, Y., Shi, W. D., Ji, L. L., Yang, Y. F., & Ping, Y. F. (2018). Numerical simulation of transient flow field in a mixed-flow pump during starting period. *International Journal of Numerical Methods for Heat & Fluid Flow*, *28*(4), 927-942. <https://doi.org/10.1108/HFF-06-2017-0220>
- Li, X. J., Chen, B., Luo, X. W., & Zhu, Z. C. (2020). Effects of flow pattern on hydraulic performance and energy conversion characterisation in a centrifugal pump. *Renewable Energy*, *151*, 475-487. <https://doi.org/10.1016/j.renene.2019.11.049>
- Li, X. J., Yuan, S. Q., Pan, Z. Y., Li, Y. L., & Yan, J. (2012). Realization and application evaluation of near-wall mesh in centrifugal pumps. *Transaction of the Chinese Society Agricultural Engineering*, *28*(20), 67-72.
- Liu, H. L., Wang, Y., Liu, D. X., Yuan, S. Q., & Wang, J. (2013). Assessment of a turbulence model for numerical predictions of sheet-cavitating flows in centrifugal pumps. *Journal of Mechanics science and Technology*, *27*(9), 2743-2750. <https://doi.org/10.1007/s12206-013-07208>
- Olimstad, G., Osvoll, M., & Finstad, P. H. E. (2018). Very low specific speed centrifugal pump-hydraulic design and physical limitations. *ASME. Journal of Fluids Engineering*, *140*(7), 071403. <https://doi.org/10.1115/1.4039250>
- Parikh, T., Mansour, M., & Thévenin, D. (2020). Investigations on the effect of tip clearance gap and inducer on the transport of air-water two-phase flow by centrifugal pumps. *Chemical Engineering Science*, *218*, 115554. <https://doi.org/10.1016/j.ces.2020.115554>
- Rezghi, A., & Riasi, A. (2016). Sensitivity analysis of transient flow of two parallel pump-turbines operating at runaway. *Renewable Energy*, *86*, 611-622. <https://doi.org/10.1016/j.renene.2015.08.059>
- Shao, C. L., He, A. X., Zhang, Z. Y., & Zhou, J. F. (2019). Study on the transition process of a molten salt pump transporting media with crystalline particles by modeling test and numerical simulation. *International Journal of Numerical Methods for heat & Fluid Flow*, *29*(9), 3263-3289. <https://doi.org/10.1108/HFF-12-2018-0807>
- Shao, C. L., Zhou, J. F., & Cheng, W. J. (2015). Experimental and numerical study of external performance and internal flow of a molten salt pump that transports fluids with different viscosities. *International Journal of Heat and Mass Transfer*, *89*, 627-640. <https://doi.org/10.1016/j.ijheatmasstransfer.2015.05.087>
- Wang, J., Wang, Y., Liu, H. L., Si, Q. R., & Dular, M. (2018). Rotating corrected-based cavitation model for a centrifugal pump. *ASME. Journal of Fluids Engineering*, *140*(11), 11301. <https://doi.org/10.1115/1.4040068>
- Wang, Y., Chen, J., Liu, H. L., Shao, C., & Zhang, X. (2017). Transient characteristic analysis of ultra-low specific-speed centrifugal pumps during startup period under shut-off condition. *Transactions of the Chinese Society of Agricultural Engineering*, *33*(11), 68-74. <https://doi.org/10.11975/j.issn.1002-6819.2017.11.009>
- Yan, S. N., Luo, X. Q., Zhang, L. F., Feng, J. J., Zhu, G. J., Chen, S. L., He, D. H., & Li, C. H. (2019). Influence of inlet gas volume fraction on performance of a gas-liquid centrifugal pump. *IOP Conference Series: Earth and Environmental Science*, *240*, 062059. <https://doi.org/10.1088/1755-1315/240/6/062059>
- Yu, Z. Y., & Liu, Y. (2013). Characteristic analysis of unsteady gas-liquid two-phase flow in a multiphase rotodynamic pump. *Transactions of the Chinese Society for Agricultural Machinery*, *44*(5), 66-69. <https://doi.org/10.6041/j.issn.1000-1298.2013.05.013>
- Yuan, J. P., Zhang, K. Y., Si, Q. R., Zhou, B. L., Tang, Y. F., & Jin, Z. K. (2017). Numerical investigation of gas-liquid two-phase flow in centrifugal pumps based on inhomogeneous model. *Transactions of the Chinese Society for Agricultural Machinery*, *48*(1), 89-95. <https://doi.org/10.6041/j.issn.1000-1298.2017.01.012>
- Zhang, Y. (2020). Study on transient characteristics of centrifugal pumps during power-off runaway transient process. Xi An, Xi'an University of Technology. <https://doi.org/10.27398/d.cnki.gxalu.2020.000473>
- Zhang, Y. L., Xiao, J. J., Cui, B. L., & Zhu, Z. C. (2014). Simulation of transient behavior in prototype centrifugal pump during rapid regulating flow rate. *Transactions of the Chinese Society of Agricultural Engineering*, *30*(11), 68-75.

<https://doi.org/10.3969/j.issn.1002-6819.2014.11.009>

- Zhang, Y. L., Zhu, Z. C., Cui, B. L., Li, Y., & Tao, H. R. (2012). Numerical simulation of unsteady flow in centrifugal pump during stopping period. *Journal of Engineering Thermophysics*, *33*(12), 2096-2099.
- Zhao, L., Chang, Z., Zhang, Z. D., Huang, R., & He, D. H. (2021). Visualization of gas-liquid flow pattern in a centrifugal pump impeller and its influence on the pump performance. *Measurement: Sensors*, *13*, 100033.
<https://doi.org/10.1016/j.measen.2020.100033>
- Zhao, W. G., & Zhao, G. S. (2018). Numerical investigation on the transient characteristics of sediment-laden two-phase flow in a centrifugal pump. *Journal of Fluid Mechanics science and Technology*, *32*(1), 167-176.
<https://doi.org/10.1007/s12206-017-1218-6>
- Zhou, L., Han, Y., Lv, W. N., Yang, Y., Zhu, Y., & Song X. Y. (2020). Numerical calculation of energy performance and transient characteristics of centrifugal pump under gas-liquid two-phase condition. *Micromachines*, *11*(8), 728-742.
<https://doi.org/10.3390/mi11080728>
- Zhou, P. J., Wang, F. J., & Mou, J. G. (2017). Investigation of rotating stall characteristics in a centrifugal pump impeller at low flow rates. *Engineering Computations*, *34*(6), 1989-2000.
<https://doi.org/10.1108/EC-05-2016-0167>